Astronomy & Astrophysics manuscript no. output
August 18, 2026

The *JWST* Proto-PAH project: Aromatic backbones with extensive aliphatic substitution account for both the aromatic and aliphatic emission

N. Clark[1,2], E. Peeters[1,2], J. Cami[1,2], G. C. Sloan[3,4], K. Volk[3], K. E. Kraemer[5], H. L. Dinerstein[6], ,M. A. Gómez-Muñoz[7,8,9], G. M. Wahlgren[3], N. C. Sterling[10], A. Ricca[11,12], A. A. Zijlstra[13], J. Li[14,15], M. Matsuura[16], D. A. García-Hernández[14,15], R. Sahai[17], B. Aringer[18,19], C. Bhatt[1,2], J. Bernard-Salas[20,21], D. Das[1], A. Manchado[14,15,22]

(Affiliations can be found after the references)

Received xxx; accepted xxx

ABSTRACT

We find that the aromatic and aliphatic emission bands in four carbon-rich post-AGB stars with Class D emission arise from a single carrier population: extensive aliphatic decoration of an aromatic skeleton, i.e. molecules with a coherent aromatic backbone and an unusually high aliphatic content. This conclusion is based on JWST NIRSpec and MIRI/MRS spectroscopy, covering 2.88–28.7 μm.
The aliphatic 3.4 μm feature is stronger than the aromatic 3.3 μm feature, reversing the ratio seen in sources with typical Polycyclic Aromatic Hydrocarbon (PAH) emission. If the aromatic emission arose from nominal PAHs, the 3.3 μm feature, unavailable in previous observations, together with the mid-IR aromatic features would constrain them to be large ($\gtrsim$200 carbon atoms), compact, and at least partially ionized; properties that predict a strong 8.6 μm feature. Yet the 8.6 μm feature is weak or absent in all four sources, ruling out any as the source of the aromatic emission, which must instead arise from the same carriers as the aliphatic emission. The position of the 6.9 μm feature and the broadened 11–14 μm out-of-plane emission independently support this. The CH_2 and CH_3 feature strengths vary across the sample, with the Class D2 sources showing higher CH_3 content. These carriers are far more aliphatic than the PAHs of planetary nebulae and the ISM, yet retain the aromatic skeleton that produces their aromatic features.

Key words. Stars: AGB and post-AGB - circumstellar matter - astrochemistry - ISM: molecules - Techniques: spectroscopic

1. Introduction

The winds of carbon stars produce an abundance of carbonaceous species ranging from single-carbon molecules to amorphous carbon grains (e.g., Martin & Rogers 1987; Cernicharo et al. 2000; Groenewegen et al. 2009). As these stars evolve rapidly past the asymptotic giant branch (AGB) and into carbon-rich planetary nebulae (PNe), their molecular inventory changes significantly under the increasingly harsh UV radiation (van der Veen et al. 1989; Kwok et al. 1999; Sloan et al. 2007; Tielens 2008): carbon stars show emission from simple molecular species, while PNe show more complex molecules such as polycyclic aromatic hydrocarbons (PAHs) and fullerenes (Allamandola et al. 1989; Cernicharo et al. 2000; Groenewegen et al. 2009; Cami et al. 2010). The post-AGB phase allows us to probe this transition in detail.

The PAH emission features (also known as the unidentified infrared bands or UIRs, e.g., Allamandola et al. 1989) are classified according to their spectral characteristics, which provides a diagnostic of the chemical structure of the underlying PAH carriers (Peeters et al. 2002; van Diedenhoven et al. 2004; Matsuura et al. 2014; Sloan et al. 2014). PAH features are classified as A, B, or C, with class B being the most common in PNe.

Several carbon-rich post-AGB stars in the Magellanic Clouds exhibit peculiar spectra inconsistent with any of the three PAH classes (Sloan et al. 2014; Matsuura et al. 2014). In particular, the 7–9 μm emission is exceptionally broad, and no "valley" is observed between the typical 7.7 and 8.6 μm features; these sources were therefore designated class D. Little is known about the nature of these carriers; however, they have been suggested to represent an intermediate stage in the chemical evolution from the carbonaceous species of AGB stars to the fully-formed PAHs of PNe (Matsuura et al. 2014; Sloan et al. 2014). Given that these carriers may represent species evolving into the familiar PAHs of PNe, we refer to them as "Proto-PAHs".

Previous Spitzer observations were limited by the low spectral resolution and the lack of near-IR coverage, but still made significant progress in characterizing this emission (Sloan et al. 2014). Notably, strong features at 6.9 and 7.25 μm were identified and attributed to dust grains containing large amounts of aliphatic content (Sloan et al. 2014), and emission inconsistent with PAHs was identified in the 11–14 μm range (Sloan et al. 2014; Matsuura et al. 2014). The absence of near-IR coverage, however, left the aromatic component of these sources unconstrained: without the 3.3 μm feature, the size, charge and structure of the aromatic carriers could not be determined, and it remained unclear whether the aliphatic and aromatic emission arise from the same species or from two co-located populations. In this work we exploit the near-infrared coverage and higher spectral resolution of JWST to resolve this question. We show that the aliphatic and aromatic emission arise from a single population of carriers: extensive aliphatic decoration of an aromatic skeleton.

2. Observations and Data Reduction

This paper uses spectroscopic observations taken with the *JWST* (Gardner et al. 2023) NIRSpec (Jakobsen et al. 2022;

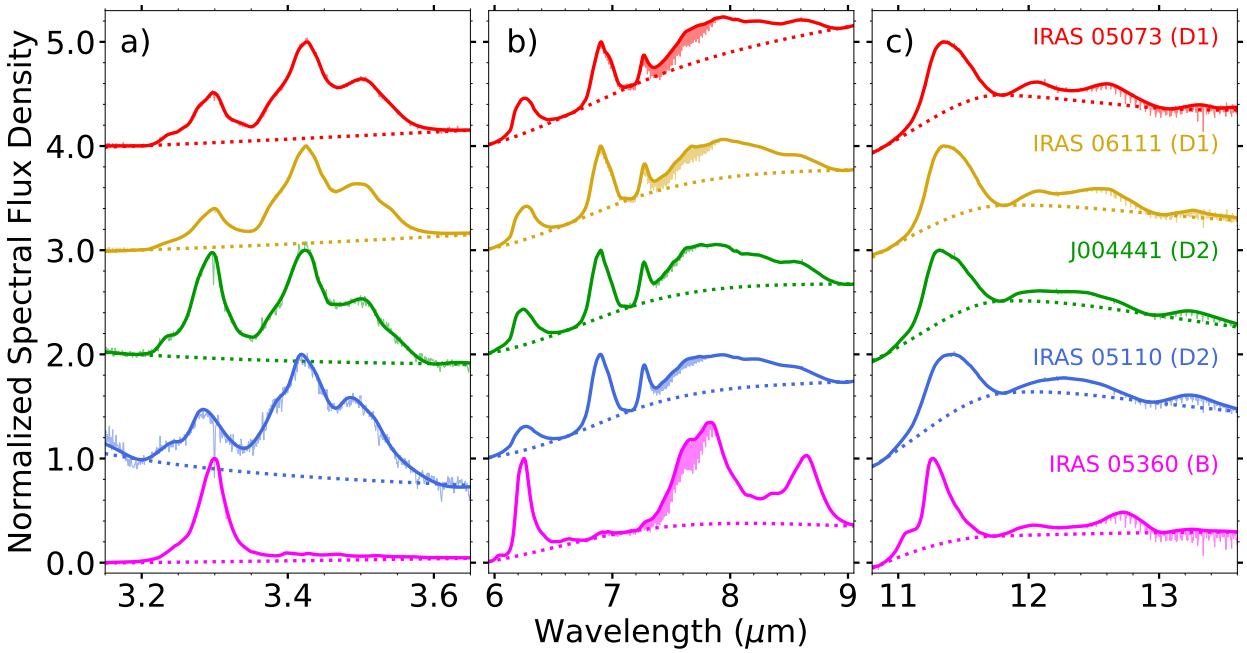

Fig. 1. The spectra, scaled and offset, with adopted continuum estimates (dotted lines). The observed spectra are shown as thin colored lines, and those with molecular features removed as thick lines of the same color. IRAS 05073 (Class D1, scale: 353.01, offset: 4) is shown in red, IRAS 06111 (Class D1, scale: 190.88, offset: 3) in orange, J004441 (Class D2, scale: 749.73, offset: 2) in green, IRAS 05110 (Class D2, scale: 880.88, offset: 1) in blue, and IRAS 05360 (Class B, scale: 25.03, offset: 0) in purple. IRAS 05360 (Class B) is included as a reference for typical PAH emission in a post-AGB/PN environment. Panel a) covers the 3–4 μm range, containing emission from C–H stretching modes. Panel b) covers the 6–9 μm range, containing emission from C–H aliphatic bending, C–C stretching and C–H in-plane bending modes. Panel c) covers the 11–15 μm range, containing emission from aromatic C–H out-of-plane bending (OOP) modes.

Böker et al. 2023) and Mid-Infrared Instrument (MIRI, Wright et al. 2023), as part of the GO3 program 4678 (PI: G. Sloan). For NIRSpec the fixed slit S200A1 (0.2″ width), G395H grating, and F290LP filter is used, yielding 2.88–5.12 μm spectra with a gap at 3.68–3.79 μm at a spectral resolution of 2700). For MIRI, data was obtained using the Medium Resolution Spectrometer (MRS) (Argyriou et al. 2023). The MRS comprises four integral field units (channels 1–4), and three grating settings (SHORT, MEDIUM, and LONG, also known as A, B, C), giving 4.9–27.9 μm spectra at a spectral resolution of 2000–3000. Further details on the observations and information on the data reduction, including the application of the point fixed-pattern correction (PFPC, Gordon & Law 2026), are provided in Sloan et al. (submitted).

The focus of this work is on the spectra of four carbon-rich post-AGB stars previously classified as having Class D PAH emission in the 6–9 μm range (Matsuura et al. 2014; Sloan et al. 2014): IRAS 05073–6752[1], IRAS 06111–7023, 2MASS J00444111–7321361, and IRAS 05110–6616. Three targets are located in the Large Magellanic Cloud (LMC), while J004441 is in the Small Magellanic Cloud (SMC). Of these, IRAS 05073 and IRAS 06111 were further classified as D1 (having bands with peak wavelength near 11.3, 12.0, and 12.7 μm), while J004441 and IRAS 05110 were classified as D2 (having bands with peak wavelength near 11.4, 12.4, 13.2 μm, Matsuura et al. 2014; Sloan et al. 2014). Also included is IRAS 05360–7121 (in the LMC) as a reference; in contrast to the Class D features, IRAS 05360 has Class B features (Matsuura et al. 2014; Sloan et al. 2014), with strong, easily recognizable PAH features at 3.3, 6.2, 7.7, 8.6, and 11.24 μm (Fig. 1).

[1] short-form names of these targets are used throughout for brevity

The spectra have an abundance of narrow molecular emission and absorption features (Sloan et al., submitted). These are removed to improve the clarity of our figures, treating each as un-blended, with the exception of the 3.0–3.15 and 14–15 μm ranges. In these ranges, the blended features are replaced with a cubic spline, smoothly connecting the spectrum on either side. To isolate the emission features from the underlying emission, a cubic spline is fit to the data to serve as a continuum (see Table A.1 for details). The fitted continua include broad plateau features common in PAH-emitting sources, extending over the 6–9 and 11–14 μm ranges (Fig. 1).

3. Results

Fig. 1 illustrates the spectral differences between Class D and Class B sources (Matsuura et al. 2014; Sloan et al. 2014). One key distinction is the prominence of aliphatic emission in Class D spectra, with strong features at 3.4, 6.9, and 7.25 μm.

Such aliphatic emission is typically a fraction of the strength of the aromatic emission, and has previously been associated with aliphatic functional groups attached to larger hydrocarbon structures rather than with free carbon chains and super-hydrogenated PAHs (Bernstein et al. 1996; Joblin et al. 1996; Chiar et al. 2000; Pino et al. 2008; Carpentier et al. 2012; Jones et al. 2013); this is examined in Section 4.1. This section focuses on these three features, and the 3.3 μm feature.

3.1. Spectral Characteristics

Fig. 2 shows the normalized, continuum-subtracted 3.3, 3.4, 6.9, and 7.25 μm features of the class D spectra. The profiles are

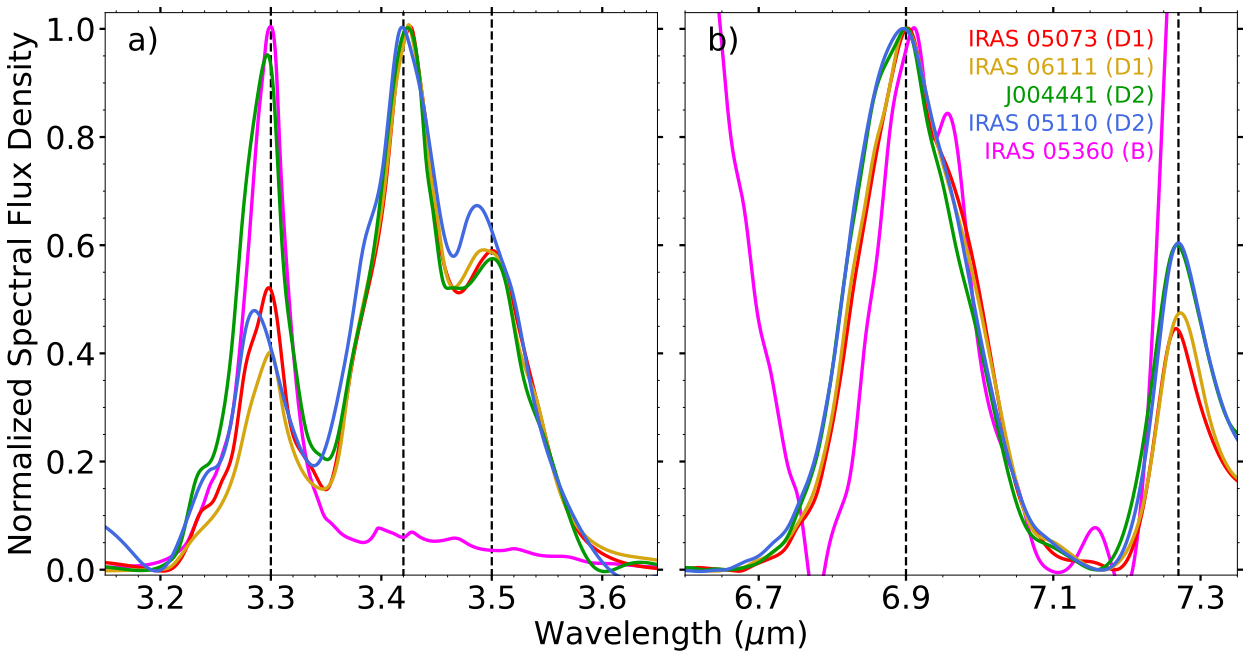

Fig. 2. Normalized, continuum-subtracted emission features. IRAS 05360 is included as a reference; its aliphatic emission is very small compared to its aromatic emission. Panel a) covers the 3.1–3.7 μm range, containing emission from C–H stretching modes, normalized to the peak emission at 3.42 μm, except for IRAS 05360, which is normalized to the peak emission at 3.30 μm. Dashed vertical lines indicate the location of 3.3 μm feature peak at 3.30 μm, and the main 3.4 μm feature peaks, at 3.42 and 3.50 μm. Panel b) covers the 6.6–7.4 μm range, containing emission primarily from C–H aliphatic bending modes, normalized to the peak emission at 6.90 μm. The aromatic 7.7 μm feature is also partially included, blending with the red wing of the 7.25 μm feature, and dominating it in the case of IRAS 05360; this spectra also has the end of a feature at 6.7 μm. Dashed vertical lines indicate the location of the 6.9 and 7.25 μm feature peaks, at 6.90 and 7.27 μm.

overall very similar, with most differences arising in the relative strengths of individual feature sub-components.

Fig. 2a shows the 3.3 and 3.4 μm features. As the spectrum of IRAS 05360 demonstrates in Fig. 2a, the 3.3 μm feature is typically much stronger than the 3.4 μm feature. In the Class D spectra, however, this is reversed: the 3.4 μm feature is consistently much stronger than the 3.3 μm feature. Overall, the 3.4 μm feature profile is similar across the Class D sources. The Class D2 source IRAS 05110 exhibits some subtle deviations: its 3.52 μm peak is enhanced relative to the 3.42 μm peak, with both located at slightly bluer wavelengths, and the more pronounced shoulder at 3.38 μm produces a slightly broader blue rise overall. More variation is seen in the peak position of the 3.3 μm feature, ranging from 3.28 μm for the Class D2 source IRAS 05110, consistent with the blue-shift seen in its 3.4 μm components, to 3.30 μm for the other sources.

The 6.9 and 7.25 μm features show similar spectral characteristics across the sources (Fig. 2b). Notably, when normalized to the 6.9 μm feature strength, the 7.25 μm features are of similar strength within the Class D2 sources, and likewise within the Class D1 sources, though the Class D1 features are overall weaker than those of the Class D2 sources. These and other key ratios are listed in Table 1.

3.2. Assignments and decomposition

Carbonaceous emission features can be broadly classified by the type of chemical bonding of the C and H responsible for them. Aromatic C–H bonds occur on sp^2-hybridized carbon in conjugated ring structures, as in PAHs; aliphatic C–H bonds occur on sp^3-hybridized carbon in non-cyclic chain structures, such as methyl (CH_3) and methylene (CH_2) groups; and olefinic C–H bonds, also sp^2-hybridized, occur on non-aromatic carbon chains containing C=C double bonds. Vibrational assignments for these modes are well established (Silverstein et al. 1963; Socrates 1980; Allamandola et al. 1989; Ristein et al. 1998; Dartois & Muñoz-Caro 2007), and these are adopted throughout; a specific reference is given only where a particular assignment is at issue. Aromatic, aliphatic, and olefinic C–H vibrational modes often overlap in wavelength. The 3.3 μm feature is primarily associated with aromatic C–H stretching, with some contribution from olefinic C–H stretching, whereas the 3.4 μm feature arises from aliphatic C–H stretching (Jourdain de Muizon et al. 1986; Geballe et al. 1992, 1994). The 6.9 and 7.25 μm features arise primarily from aliphatic C–H bending modes, with some weak aromatic and olefinic contributions between them: asymmetric bending such as scissoring modes near 6.9 μm, and symmetric bending near 7.25 μm.

To aid our analysis, the 3.3, 3.4, 6.9, and 7.25 μm features are decomposed using a series of Gaussians, each corresponding to a known C–H vibrational assignment; these decompositions are shown in Fig. 3. The fits are calculated with a linear least squares approach. To reduce degeneracy, the Gaussian components are fitted incrementally for each feature: amplitudes, widths, and peak positions were first determined for regions well represented by a single Gaussian component, with additional blended components fit subsequently. Care was also taken to ensure that components reported as weak or narrow in the literature remained so, with minimal variation in peak position and width of each component across the different sources. Table 2 lists the fitted positions, standard deviations, and vibrational modes. The integrated intensities of the components, derived from the fitting, are listed in Table A.2. This work aims to isolate the aliphatic emission from the aromatic and olefinic contributions and to resolve

Table 1. Integrated intensity ratios for key emission features and components. The intensities themselves are given in Table A.3.

Feature Ratio	IRAS 05073 (D1)	IRAS 06111 (D1)	J004441 (D2)	IRAS 05110 (D2)
3.3/11.2	0.053 ± 0.003	0.047 ± 0.002	0.085 ± 0.005	0.023 ± 0.003
6.2/11.2	0.63 ± 0.02	0.70 ± 0.02	0.68 ± 0.02	0.56 ± 0.01
3.38/3.42	0.41 ± 0.02	0.44 ± 0.01	0.50 ± 0.03	0.66 ± 0.05
7.25/6.9 aliph.	0.20 ± 0.05	0.21 ± 0.04	0.28 ± 0.01	0.28 ± 0.01
3.4 aliph./Σ(3.3, 3.4)	0.77 ± 0.03	0.81 ± 0.02	0.66 ± 0.04	0.77 ± 0.08
6.9 aliph./6.9	0.82 ± 0.04	0.83 ± 0.03	0.91 ± 0.03	0.91 ± 0.02

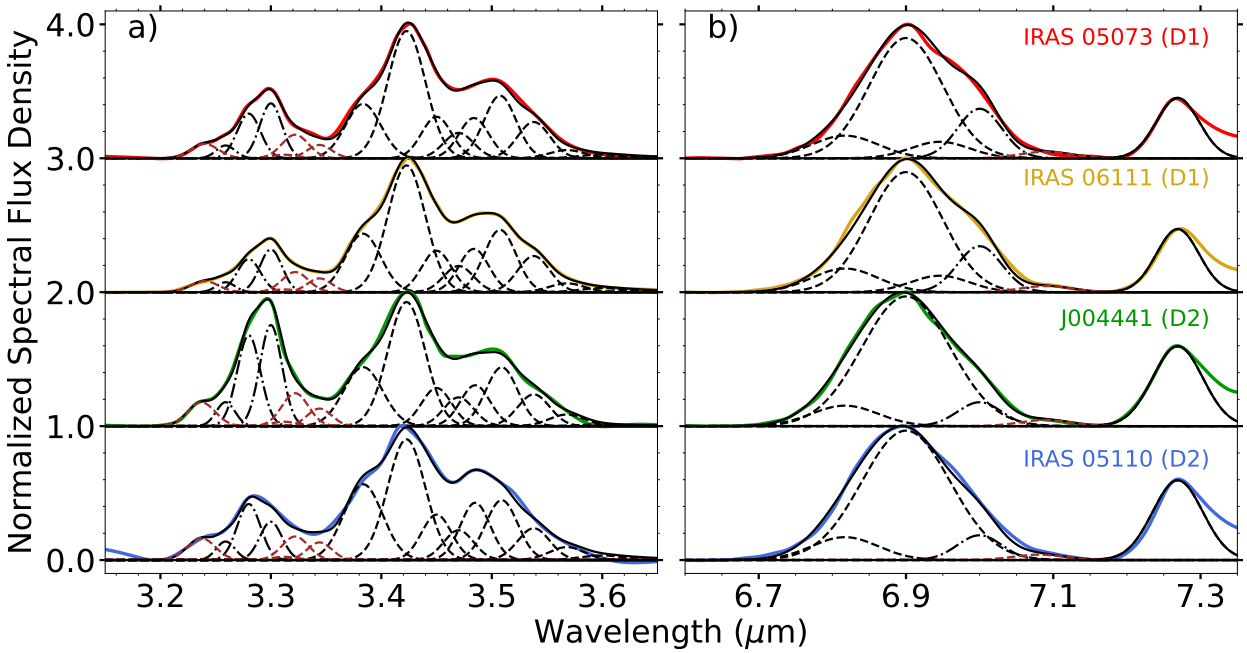

Fig. 3. Decomposition of normalized, continuum-subtracted emission features, with an offset added for clarity. Normalization is to the peak emission at 3.42 μm (panel a) and at 6.90 μm (panel b). IRAS 05073 (Class D1, scale: (a) 383.07, (b) 35.22, offset: 3) is shown in red, IRAS 06111 (Class D1, scale: (a) 206.09, (b) 16.36, offset: 2) in orange, J004441 (Class D2, scale: (a) 703.80, (b) 50.98, offset: 1) in green, and IRAS 05110 (Class D2, scale: (a) 754.13, (b) 20.35, offset: 0) in blue. Gaussians corresponding to aromatic vibrations are shown with black dash-dot lines, those corresponding to aliphatic vibrations with black dashed lines, and those corresponding to olefinic vibrations with brown dashed lines. The sum of the fitted Gaussians is shown with a solid black line.

the sub-components that constrain the CH_3/CH_2 balance and the proximity of aliphatic groups to aromatic rings. Every component does not require a unique assignment.

Gaussians corresponding to aliphatic vibrations fit the 3.4 μm feature well, while combinations of aromatic and olefinic vibrations fit the 3.3 μm band well. Of note, variation in the relative strength of the components at 3.38, and beyond 3.50 μm, recreate the observed 3.4 μm profile variations. Gaussians corresponding to aliphatic vibrations fit both the 6.9 and 7.25 μm features, although subtle variations in the 6.9 μm band arise from non-aliphatic emission. The 7.25 μm feature has a broad red wing, which we attribute to blending with the strong aromatic 7.7 μm feature (Peeters et al. 2002).

4. Discussion

4.1. A single population: aliphatic groups on an aromatic skeleton

The strong aliphatic features in these sources could arise in two ways. Either the aliphatic and aromatic emission come from two independent populations – PAHs carrying few aliphatic side-groups, as is typical of astronomical PAHs (e.g. Yang et al. 2016, 2017), alongside a separate aliphatic-rich component – or they come from a single population of molecules bearing both aromatic and aliphatic C–H bonds. For the remainder of this paper, we refer to PAHs carrying few aliphatic side-groups, as is typical of astronomical PAHs, as 'nominal PAHs'. We show below that the observations require the second option: no distribution of nominal PAHs can account for the observed aromatic emission, while both the observed aromatic and aliphatic emission are consistent with a single carrier population.

First, we consider the population of nominal PAHs needed to produce the observed aromatic features, and find that no such distribution of nominal PAHs. The size, charge, and edge structure are each considered in turn. The ratio of the 3.3 and 11.2 μm bands (hereafter 3.3/11.2 ratio) traces the size of PAHs (e.g., Schutte et al. 1993; Ricca et al. 2012; Croiset et al. 2016; Knight et al. 2021). Using the diagnostics involving the 3.3 and 11.2 μm features from Maragkoudakis et al. (2020), adjusted for the anharmonic correction of Lemmens et al. (2023), the observed ratios (Table 1) indicate that the PAHs contain at least 200 carbon atoms. The relative strengths of the 6.2 and 7.7 μm features probe the PAH charge (Leger & Puget 1984; Allamandola et al. 1989; Galliano et al. 2008). The 6.2 μm feature is strong relative to the 11.2 μm feature (6.2/11.2 = 0.56–

Table 2. Fitting parameters of the Gaussian decompositions. Each component is assigned a vibrational bond type – olefinic (Olef.), aromatic (Arom.), or aliphatic (Aliph.) – along with a more specific vibrational assignment. Vibrational assignments are abbreviated as follows: stretching (str.), bending (bnd.), symmetric (sym.), and asymmetric (asym.). All parameters are in μm. Any variation in fitting parameters across sources is noted.

Peak Position (Standard Deviation)	Vibrational Assignment
3.3, 3.4 μm features	
3.240 (0.0125) [1]	Olef. CH_2 asym. str.
3.259 (0.0085)	Arom. CH str.
3.280 (0.0105)	Arom. CH str.
3.300 (0.0100)	Arom. CH str.
3.312 (0.0120)	Olef. CH str.
3.322 (0.0120)	Olef. CH str.
3.344 (0.0110)	Olef. CH_2 sym. str.
3.3835 (0.0160) [2]	Aliph. CH_3 asym. str.
3.4228 (0.0170)	Aliph. CH_2 asym. str.
3.450 (0.0135)	Aliph. CH str.
3.470 (0.0135)	Aliph. CH str.
3.4838 (0.0135) [3]	Aliph. CH_3 sym. str.
3.5075 (0.0145) [4]	Aliph. CH_2 sym. str.
3.538 (0.0145)	Aliph. CH_2 sym. str.
3.568 (0.0160)	Aliph. str. red wing
3.600 (0.0200)	Aliph. str. red wing
3.640 (0.0240)	Aliph. str. red wing
6.9, 7.25 μm features	
6.817 (0.045)	Aliph. CH_2, CH_3 asym. bnd.
6.900 (0.050) [5]	Aliph. CH_2, CH_3 asym. bnd.
6.946 (0.040)	Aliph. CH_2, CH_3 asym. bnd.
7.000 (0.0300)	Arom. CH bnd.
7.090 (0.0350) [6]	Olef. CH_2 bnd.
7.269 (0.0290) [7]	Aliph. CH_3 sym. bnd.

[1] Class D2: peak at 3.237
[2] Class D2: std. dev. of 0.0175
[3] Class D2: peak at 3.4850
[4] Class D2; peak at 3.5085
[5] Class D2; std. dev. of 0.051
[6] IRAS 05110: peak at 7.080
[7] Class D2: std. dev. of 0.0295

0.70; see Table 1), indicating that the PAHs are at least partially ionized (Maragkoudakis et al. 2020). The 7.7 μm feature is blended with the red wing of the 7.25 μm aliphatic feature and contaminated by molecular absorption, so we do not attempt to measure it; its strength, however, is evident in Fig. 1. The relative strength of the 11–14 μm features probes the edge structure of PAHs (Hony et al. 2001; Khan et al. 2025). Since the 11.2 μm feature is strong relative to the 12.7 and 13.5 μm features (Fig. 1), these PAHs are compact, consisting mostly of straight edges. Large, compact, ionized PAHs are expected to produce a strong 8.6 μm PAH feature (Bauschlicher et al. 2008, 2009; Ricca et al. 2012). Yet the 8.6 μm feature is weak or absent in all four sources. The aromatic features therefore cannot be produced by any distribution of nominal PAHs: the very properties required to explain the 3.3, 6.2, 7.7 and 11.2 μm emission predict a strong 8.6 μm feature that is weak or absent.

We next consider the 6.9 μm feature, attributed to aliphatic C–H asymmetric bending, specifically a C–H scissoring mode (Silverstein et al. 1963; Socrates 1980; Allamandola et al. 1989; Ristein et al. 1998; Dartois & Muñoz-Caro 2007). The position of this feature depends on the chemical structure surrounding the aliphatic C–H bond undergoing the scissoring motion — specifically, whether it occurs on an isolated aliphatic chain or adjacent to an aromatic ring. For C–H scissoring modes on aliphatic chains, the feature is located at 6.82 μm. However, when the aliphatic C–H scissoring mode occurs adjacent to an aromatic ring, the feature is red-shifted to 6.9 μm (Colthup et al. 1990; Sandford et al. 2013; Materese et al. 2017). The decomposition of the 6.9 μm feature in each object shows that the majority of the emission is centered at 6.9 μm, with only a small contribution from emission located at 6.82 μm. We thus conclude that the majority of the aliphatics responsible for the 6.9 μm feature are adjacent to aromatic rings.

Lastly, we consider the emission in the 11–14 μm range. For PAHs consisting only of aromatic bonds, this emission arises from C–H out-of-plane bending (OOP) modes (Leger & Puget 1984; Allamandola et al. 1989; Hudgins & Allamandola 1999; Hony et al. 2001). There is no expected emission in this wavelength range from aliphatics or olefinics (Colthup et al. 1990; Sandford et al. 2013; Dartois et al. 2020). Thus, under the two-population hypothesis, all distinct emission features in the 11–14 μm range would be attributed to the PAHs. Molecules with aromatic rings bearing C–H bonds and aliphatic substituents on other rings still produce OOP features. However, the addition of aliphatics breaks the vibrational coupling of the OOP modes, resulting in emission across the 11–14 μm range that becomes increasingly spread out and blended (Colthup et al. 1990; Sandford et al. 2013; Dartois et al. 2020). This is precisely what is observed in the Class D spectra (Fig. 1). For example, the 11.2 μm PAH feature, which typically peaks between 11.20 and 11.25 μm, is here shifted to 11.33 μm, and has a much broader red wing than is typical. Additionally, emission is present at 12.4 and 13.2 μm, that have not been attributed to PAH OOP modes (Hony et al. 2001; Matsuura et al. 2014; Khan et al. 2025), and has previously been observed in spectra with strong aliphatic 6.9 and 7.25 μm features (Sloan et al. 2014; Matsuura et al. 2014). This broadening and blending of the OOP features in the Class D spectra therefore also supports the single-population scenario.

As a final note, we attribute the variation in aliphatic emission among the Class D sources to differences in the type of aliphatic content present. As an example, aliphatic CH_3 stretching modes produce emission at 3.38 μm, while CH_2 stretching modes produce emission at 3.42 μm. Similarly, the 7.25 μm feature is primarily attributed to CH_3 bending modes, whereas both CH_2 and CH_3 bending modes contribute to 6.9 μm emission (Colthup et al. 1990; Ristein et al. 1998; Dartois & Muñoz-Caro 2007). The Class D1 sources have smaller 3.38/3.42 μm component ratios than the Class D2 sources, and the 7.25/6.9 μm ratio is also larger in the Class D2 sources. Both lines of evidence suggest that the Class D2 sources have relatively higher CH_3 content.

4.2. The structure of the Proto-PAH carriers

Large molecules or dust grains with mixed aromatic and aliphatic content have been proposed as carriers of the UIRs in place of PAHs (see e.g., Duley & Williams 1981; Kwok & Zhang 2011). We briefly discuss these alternatives before turning to the implications for our sources.

While carbonaceous dust grains are excellent candidate carriers to explain the aliphatic *absorption* features seen along some lines of sight (Sandford et al. 1991; Pendleton et al. 1994; Pendleton & Allamandola 2002; Dartois & Muñoz-Caro 2007; Chiar et al. 2013). However, they are less suited to explain the

UIR *emission* characteristics. The UIR emission points to carriers of much smaller heat capacity, which can be stochastically heated to high temperatures by individual photons, rather than reaching the lower equilibrium temperatures of bulk grains (e.g., Sellgren 1984; Draine & Li 2001; Tielens 2008).

The emission spectra provide additional constraints on the molecular structure of the carriers. In the astronomical context, a PAH molecule is a coherent aromatic skeleton, possibly bearing aliphatic substituents such as methyl or methylene side groups or with super-hydrogenated edges or surfaces (a "dirty" PAH; see e.g., Allamandola et al. 1989; Hudgins & Allamandola 1999; Tielens 2008). Such a species has a discrete vibrational spectrum and a low heat capacity; under stochastic heating it emits the aromatic features at their characteristic positions, with aliphatic features appearing as satellites (see e.g., Allamandola et al. 1999; Bauschlicher et al. 2010; Boersma et al. 2014; Rosenberg et al. 2014; Mattioda et al. 2020). A mixed-aromatic organic nanoparticle (MAON), by contrast, is an internally bulk-structured nanoparticle: a three-dimensional amorphous network of small aromatic units cross-linked by aliphatic chains, in which the structure is dominated by the aliphatic linkages rather than by a coherent aromatic backbone (Kwok & Zhang 2011). The distinction is therefore one of structure, not composition.

The sharpness and fixed positions of the 6.2, 7.7 and 11.2 μm features require a coherent aromatic skeleton, and the low aliphatic fractions inferred for the general UIR population (~2–9%; Li & Draine 2012; Yang et al. 2016, 2017) place those carriers firmly on the (dirty-)PAH side of this divide. Experimental and theoretical PAH spectra compare well to the observed UIRs (see e.g., Allamandola et al. 1999; Bauschlicher et al. 2010; Mattioda et al. 2020), further supporting this interpretation.

Because a MAON is an aliphatic-dominated network, its emission spectrum is necessarily dominated by the aliphatic features rather than by the aromatic-dominated feature set that defines the UIRs. To the best of our knowledge, no spectrum of a MAON has yet been published; the mixed-carrier models draw their plausibility from bulk hydrogenated amorphous carbon (HAC) and quenched carbonaceous composite (QCC) laboratory analogues, without spectroscopically modeling the proposed particle itself. We therefore do not adopt the mixed-carrier hypothesis for the general UIR features.

The four sources we study in this paper, however, are precisely where this distinction becomes interesting. They are at an aliphatic-rich, transitional phase of post-AGB evolution, in which aliphatic features weaken relative to the aromatic ones as sources evolve towards the PN stage (Joblin et al. 1996; Kwok et al. 1999). Their aliphatic content – evident in the reversed 3.4/3.3 ratio and the exceptional strength of the 6.9 μm feature – is far higher than in general UIR sources, placing them, among known carriers, closest to the aliphatic-rich regime the mixed-carrier models describe. Yet they retain sharp aromatic features at 3.3, 6.2, 7.7 and 11.2 μm – the signature of an intact aromatic skeleton. The weakness or absence of the 8.6 μm feature, far from contradicting this, is precisely what distinguishes these carriers from nominal PAHs. A critical open question is whether these carriers approach the MAON-like structural regime, or remain aromatic-skeleton molecules carrying an unusually heavy aliphatic decoration. A quantitative determination of their aliphatic fraction, and the structural questions it raises, will be the subject of a forthcoming paper.

5. Conclusions

We investigate JWST NIRSpec and MIRI/MRS spectroscopy of four carbon-rich post-AGB stars with Class D emission, covering the 3-–4 μm region for the first time in these objects. We find that the aliphatic and aromatic emission arise from a single population of carriers: extensive aliphatic decoration of an aromatic skeleton, i.e. molecules with a coherent aromatic backbone and an unusually high aliphatic content.

The 3.4 μm aliphatic feature is stronger than the neighboring 3.3 μm aromatic feature, a reversal of the ratio seen in typical PAH sources, and the 6.9 and 7.25 μm features likewise dominate their surroundings. We decompose the primarily aliphatic 3.4, 6.9, and 7.25 μm features and the primarily aromatic 3.3 μm feature into components consistent with established aromatic, aliphatic, and olefinic C–H vibrational assignments.

The aromatic features require carriers that are large, compact, and at least partially ionized; such PAHs should produce a strong 8.6 μm feature. Its weakness or absence in all four sources rules out any distribution of nominal PAHs as the source of the aromatic emission in these targets, which must therefore arise from the same carriers as the aliphatic emission. This conclusion is supported by the position of the 6.9 μm feature, indicative of aliphatic groups adjacent to aromatic rings, and by the 11–14 μm emission, consistent with aromatic C–H out-of-plane bending modes strongly perturbed by nearby aliphatic structure.

We identify variation in the aliphatic emission between the Class D1 and Class D2 sources, consistent with variation in the relative CH_3/CH_2 content, and therefore in the degree of methyl substitution among the carriers in these sources.

These carriers are far more aliphatic than the PAHs seen in planetary nebulae and the interstellar medium, yet retain the aromatic skeleton that produces their aromatic features. Further observations of additional Proto-PAH candidate sources, along with complementary laboratory and theoretical spectroscopy, will help clarify the origin and fate of this aliphatic-rich material.

Acknowledgements. This work is based on observations made with the NASA/ESA/CSA James Webb Space Telescope. All of the data presented in this article were obtained from the Mikulski Archive for Space Telescopes (MAST) at the Space Telescope Science Institute. These observations are associated with program #4678 (DOI: 10.17909/zs5n-2t21). N.C., E.P., J.C., C.B., and D.D. acknowledge support from the Canadian Space Agency (CSA, 24JWGO3B01), and the Natural Sciences and Engineering Research Council of Canada. Support for US investigators (G.C.S., H.L.D., K.E.K., R.S., N.S., and G.M.W.) in program #4678 was provided by NASA through a grant from the Space Telescope Science Institute, which is operated by the Association of Universities for Research in Astronomy, Inc., under NASA contract NAS 5-03127. J. L., D.A.G.H. and A.M. acknowledge support from the State Research Agency (AEI) of the Spanish Ministry of Science, Innovation, and Universities (MICIU) of the Government of Spain, and the European Regional Development fund (ERDF), under grant PID2023-147325NB-I00/AEI/10.13039/501100011033. This publication is based upon work from COST Action CA21126 - Carbon molecular nanostructures in space (NanoSpace), supported by COST (European Cooperation in Science and Technology). M.A.G.M. acknowledges being funded by the European Union (ERC, CET-3PO, 101042610). Views and opinions expressed are, however, those of the author(s) only and do not necessarily reflect those of the European Union or the European Research Council Executive Agency. Neither the European Union nor the granting authority can be held responsible for them. M.A.G.M. also acknowledges financial support from grant CEX2024-001451-M funded by MICIU/AEI/10.13039/501100011033. R.S.'s contribution to the research described here was carried out at the Jet Propulsion Laboratory, California Institute of Technology, under a contract with NASA (80NM0018D0004), and partially funded by award JWST-GO-04678 from the STScI under NASA contract NAS5-03127.

References

Allamandola, L. J., Hudgins, D. M., & Sandford, S. A. 1999, ApJ, 511, L115
Allamandola, L. J., Tielens, A. G. G. M., & Barker, J. R. 1989, Astrophysical Journal Supplement Series (ISSN 0067-0049), 71, 733
Argyriou, I., Glasse, A., Law, D. R., et al. 2023, A&A, 675, A111
Bauschlicher, Jr., C. W., Boersma, C., Ricca, A., et al. 2010, ApJS, 189, 341
Bauschlicher, Charles W., J., Peeters, E., & Allamandola, L. J. 2008, ApJ, 678, 316
Bauschlicher, Charles W., J., Peeters, E., & Allamandola, L. J. 2009, ApJ, 697, 311
Bernstein, M. P., Sandford, S. A., & Allamandola, L. J. 1996, ApJ, 472, L127
Boersma, C., Bauschlicher, Jr., C. W., Ricca, A., et al. 2014, ApJS, 211, 8
Böker, T., Beck, T. L., Birkmann, S. M., et al. 2023, PASP, 135, 038001
Cami, J., Bernard-Salas, J., Peeters, E., & Malek, S. E. 2010, Science, 329, 1180
Carpentier, Y., Féraud, G., Dartois, E., et al. 2012, A&A, 548, A40
Cernicharo, J., Guélin, M., & Kahane, C. 2000, A&AS, 142, 181
Chiar, J. E., Tielens, A. G. G. M., Adamson, A. J., & Ricca, A. 2013, ApJ, 770, 78
Chiar, J. E., Tielens, A. G. G. M., Whittet, D. C. B., et al. 2000, ApJ, 537, 749
Colthup, N. B., Daly, L. H., & Wiberley, S. E. 1990, Introduction to Infrared and Raman Spectroscopy (Academic Press)
Croiset, B. A., Candian, A., Berné, O., & Tielens, A. G. G. M. 2016, A&A, 590, A26
Dartois, E., Charon, E., Engrand, C., Pino, T., & Sandt, C. 2020, A&A, 637, A82
Dartois, E. & Muñoz-Caro, G. M. 2007, A&A, 476, 1235
Draine, B. T. & Li, A. 2001, ApJ, 551, 807
Duley, W. W. & Williams, D. A. 1981, MNRAS, 196, 269
Galliano, F., Madden, S. C., Tielens, A. G. G. M., Peeters, E., & Jones, A. P. 2008, ApJ, 679, 310
Gardner, J. P., Mather, J. C., Abbott, R., et al. 2023, PASP, 135, 068001
Geballe, T. R., Joblin, C., D'Hendecourt, L. B., et al. 1994, ApJ, 434, L15
Geballe, T. R., Tielens, A. G. G. M., Kwok, S., & Hrivnak, B. J. 1992, ApJ, 387, L89
Gordon, K. D. & Law, D. R. 2026, ApJ, submitted
Groenewegen, M. A. T., Sloan, G. C., Soszyński, I., & Petersen, E. A. 2009, A&A, 506, 1277
Hony, S., Van Kerckhoven, C., Peeters, E., et al. 2001, A&A, 370, 1030
Hudgins, D. M. & Allamandola, L. J. 1999, ApJ, 516, L41
Jakobsen, P., Ferruit, P., Alves de Oliveira, C., et al. 2022, A&A, 661, A80
Joblin, C., Tielens, A. G. G. M., Allamandola, L. J., & Geballe, T. R. 1996, ApJ, 458, 610
Jones, A. P., Fanciullo, L., Köhler, M., et al. 2013, A&A, 558, A62
Jourdain de Muizon, M., Geballe, T. R., D'Hendecourt, L. B., & Baas, F. 1986, ApJ, 306, L105
Khan, B., Abbott, B., Peeters, E., et al. 2025, A&A, 699, A133
Knight, C., Peeters, E., Stock, D. J., Vacca, W. D., & Tielens, A. G. G. M. 2021, ApJ, 918, 8
Kwok, S., Volk, K., & Hrivnak, B. J. 1999, A&A, 350, L35
Kwok, S. & Zhang, Y. 2011, Nature, 479, 80
Leger, A. & Puget, J. L. 1984, A&A, 137, L5
Lemmens, A. K., Mackie, C. J., Candian, A., et al. 2023, Faraday Discussions, 245, 380
Li, A. & Draine, B. T. 2012, ApJ, 760, L35
Maragkoudakis, A., Peeters, E., & Ricca, A. 2020, MNRAS, 494, 642
Martin, P. G. & Rogers, C. 1987, ApJ, 322, 374
Materese, C. K., Bregman, J. D., & Sandford, S. A. 2017, ApJ, 850, 165
Matsuura, M., Bernard-Salas, J., Lloyd Evans, T., et al. 2014, MNRAS, 439, 1472
Mattioda, A. L., Hudgins, D. M., Boersma, C., et al. 2020, ApJS, 251, 22
Peeters, E., Hony, S., Van Kerckhoven, C., et al. 2002, A&A, 390, 1089
Pendleton, Y. J. & Allamandola, L. J. 2002, ApJS, 138, 75
Pendleton, Y. J., Sandford, S. A., Allamandola, L. J., Tielens, A. G. G. M., & Sellgren, K. 1994, ApJ, 437, 683
Pino, T., Dartois, E., Cao, A.-T., et al. 2008, A&A, 490, 665
Ricca, A., Bauschlicher, Charles W., J., Boersma, C., Tielens, A. G. G. M., & Allamandola, L. J. 2012, ApJ, 754, 75
Ristein, J., Stief, R. T., Ley, L., & Beyer, W. 1998, Journal of Applied Physics, 84, 3836
Rosenberg, M. J. F., Berné, O., & Boersma, C. 2014, A&A, 566, L4
Sandford, S. A., Allamandola, L. J., Tielens, A. G. G. M., et al. 1991, ApJ, 371, 607
Sandford, S. A., Bernstein, M. P., & Materese, C. K. 2013, ApJS, 205, 8
Schutte, W. A., Tielens, A. G. G. M., & Allamandola, L. J. 1993, ApJ, 415, 397
Sellgren, K. 1984, ApJ, 277, 623
Silverstein, R. M., Webster, F. X., & Kiemle, D. J. 1963, Spectrometric Identification of Organic Compounds (Wiley)
Sloan, G. C., Jura, M., Duley, W. W., et al. 2007, ApJ, 664, 1144
Sloan, G. C., Lagadec, E., Zijlstra, A. A., et al. 2014, ApJ, 791, 28
Socrates, G. 1980, Infrared Characteristic Group Frequencies (Wiley)
Tielens, A. G. G. M. 2008, ARA&A, 46, 289
van der Veen, W. E. C. J., Habing, H. J., & Geballe, T. R. 1989, A&A, 226, 108
van Diedenhoven, B., Peeters, E., Van Kerckhoven, C., et al. 2004, ApJ, 611, 928
Wright, G. S., Rieke, G. H., Glasse, A., et al. 2023, PASP, 135, 048003
Yang, X. J., Glaser, R., Li, A., & Zhong, J. X. 2016, MNRAS, 462, 1551
Yang, X. J., Glaser, R., Li, A., & Zhong, J. X. 2017, New A Rev., 77, 1

[1] Department of Physics and Astronomy, The University of Western Ontario, London, ON N6A 3K7, Canada
e-mail: nclark68@uwo.ca
[2] Institute for Earth and Space Exploration, The University of Western Ontario, London, ON N6A 3K7, Canada
[3] Space Telescope Science Institute, 3700 San Martin Drive, Baltimore, MD 21218, USA
[4] Department of Physics and Astronomy, University of North Carolina, Chapel Hill, NC 27599-3255, USA
[5] Institute for Scientific Research, Boston College, 140 Commonwealth Avenue, Chestnut Hill, MA 02467, USA
[6] Department of Astronomy, University of Texas at Austin, Austin, TX 78712, USA
[7] Departament de Física Quàntica i Astrofísica (FQA), Universitat de Barcelona (UB), c. Martí i Franquès, 1, 08028 Barcelona, Spain
[8] Institut de Ciències del Cosmos (ICCUB), Universitat de Barcelona (UB), c. Martí i Franquès, 1, 08028 Barcelona, Spain
[9] Institut d'Estudis Espacials de Catalunya (IEEC), Edifici RDIT, Campus UPC, 08860 Castelldefels (Barcelona), Spain
[10] University of West Georgia, Carrollton, GA 30118, USA
[11] NASA Ames Research Center, MS 245-6, Moffett Field, CA 94035-1000, USA
[12] Carl Sagan Center, SETI Institute, 339 Bernardo Avenue, Suite 200, Mountain View, CA 94043, USA
[13] Jodrell Bank Centre for Astrophysics, The University of Manchester, Manchester, M13 9PL, UK
[14] Instituto de Astrofísica de Canarias, C/ Via Láctea s/n, E-38205 La Laguna, Spain
[15] Departamento de Astrofísica, Universidad de La Laguna (ULL), E-38206 La Laguna, Spain
[16] Cardiff Hub for Astrophysical Research and Technology (CHART), School of Physics and Astronomy, Cardiff University, The Parade, Cardiff CF24 3AA, UK
[17] Jet Propulsion Laboratory, MS 183-900, 4800 Oak Grove Dr., California Institute of Technology, Pasadena, CA 91109, USA
[18] Theoretical Astrophysics, Department of Physics and Astronomy, Uppsala University, Box 516, 751 20 Uppsala, Sweden
[19] Department of Astrophysics, University of Vienna, Türkenschanzstraße 17, 1180 Wien, Austria
[20] ACRI-ST, Centre d'Etudes et de Recherche de Grasse (CERGA), 10 Av. Nicolas Copernic, 06130 Grasse, France
[21] INCLASS Common Laboratory, 10 Av. Nicolas Copernic, 06130 Grasse, France
[22] Consejo Superior de Investigaciones Científicas (CSIC), Spain

Appendix A: Additional Analysis Value Tables

Table A.1 lists the wavelengths for the anchor points used in the continuum determination. Tables A.2 and A.3 list the integrated intensity of the Gaussian components used in the decomposition and of the features used in the ratios of Table 1.

Table A.1. Wavelengths of the anchor points used for the continuum spline fitting for each spectra, in units of μm.

IRAS 05073 (D1)	IRAS 06111 (D1)	J004441 (D2)	IRAS 05110 (D2)	IRAS 05360 (B)
2.9066	2.9066	2.9066	2.9066	2.9066
3.1915	3.1915	3.1915	3.1915	3.1015
3.6654	3.6854	3.6654	3.6854	3.6854
3.8837	3.8837	3.8837	3.8837	3.9000
4.2851	4.2851	4.2851	4.2851	4.2480
4.6000	4.6000	4.6000	4.6000	4.6000
4.9568	4.9568	4.9568	4.9000	4.9568
5.1196	5.1196	5.1196	5.1196	5.1196
5.4795	5.4795	5.4771	5.4771	5.4681
5.9431	5.9431	5.9431	5.9000	5.9678
6.6550	6.6550	6.6550	6.6550	6.7900
7.1823	7.1600	7.1600	7.1600	7.0950
8.9163	8.9222	8.9435	8.9134	9.1580
8.9800	8.9700	9.0150	8.9800	9.2500
9.0400	9.0373	9.0597	9.0420	9.3521
9.2200	9.2200	9.1500	9.2200	9.4380
9.5750	9.5750	9.5980	9.5743	9.4390
9.9430	9.9764	9.9781	9.9430	9.9430
10.2390	10.2390	10.2230	10.2030	10.2220
10.8090	10.8950	10.7720	10.7940	10.8326
10.8810	10.9348	10.9260	10.8920	10.8682
11.7750	11.7942	11.7729	11.8049	11.7290
11.8080	11.8371	11.7960	11.8086	11.7474
13.0450	12.9960	12.9186	12.9140	13.0498
13.9900	13.7490	13.9733	13.8620	13.9352

Table A.2. Integrated intensity of the Gaussian components of each fitted feature, in units of 1×10^{-17} W/m^2.

Peak Position	Vibrational Assignment	IRAS 05073 (D1)	IRAS 06111 (D1)	J004441 (D2)	IRAS 05110 (D2)
		3.3, 3.4 μm features			
3.240	Olef. CH_2 asym. str.	0.25 ± 0.01	0.36 ± 0.01	0.23 ± 0.01	0.20 ± 0.02
3.259	Arom. CH str.	0.15 ± 0.01	0.22 ± 0.02	0.15 ± 0.01	0.11 ± 0.01
3.280	Arom. CH str.	0.64 ± 0.02	0.88 ± 0.02	0.71 ± 0.01	0.41 ± 0.03
3.300	Arom. CH str.	0.74 ± 0.02	1.07 ± 0.02	0.74 ± 0.02	0.26 ± 0.04
3.312	Olef. CH str.	0.06 ± 0.01	0.08 ± 0.01	0.04 ± 0.01	0.03 ± 0.01
3.322	Olef. CH str.	0.38 ± 0.01	0.60 ± 0.01	0.29 ± 0.01	0.19 ± 0.01
3.344	Olef. CH_2 sym. str.	0.19 ± 0.03	0.37 ± 0.02	0.14 ± 0.02	0.13 ± 0.04
3.3835	Aliph. CH_3 asym. str.	1.11 ± 0.05	2.23 ± 0.06	0.72 ± 0.04	0.86 ± 0.06
3.4228	Aliph. CH_2 asym. str.	2.70 ± 0.03	5.01 ± 0.05	1.44 ± 0.04	1.30 ± 0.05
3.450	Aliph. CH str.	0.69 ± 0.01	1.28 ± 0.02	0.34 ± 0.02	0.38 ± 0.02
3.470	Aliph. CH str.	0.42 ± 0.01	0.80 ± 0.02	0.26 ± 0.01	0.25 ± 0.01
3.4838	Aliph. CH_3 sym. str.	0.66 ± 0.02	1.31 ± 0.02	0.36 ± 0.01	0.47 ± 0.03
3.5075	Aliph. CH_2 sym. str.	1.08 ± 0.01	2.00 ± 0.02	0.55 ± 0.02	0.52 ± 0.02
3.538	Aliph. CH_2 sym. str.	0.62 ± 0.03	1.14 ± 0.03	0.29 ± 0.02	0.27 ± 0.04
3.568	Aliph. str. red wing	0.15 ± 0.02	0.30 ± 0.03	0.12 ± 0.02	0.12 ± 0.03
3.600	Aliph. str. red wing	0.09 ± 0.02	0.17 ± 0.03	0.02 ± 0.03	0.05 ± 0.03
3.640	Aliph. str. red wing	0.05 ± 0.02	0.10 ± 0.04	0.01 ± 0.02	0.03 ± 0.04
		6.9, 7.25 μm features			
6.817	Aliph. CH_2, CH_3 asym. bnd.	3.5 ± 0.2	7.9 ± 0.3	2.2 ± 0.1	6.1133 ± 0.1
6.900	Aliph. CH_2, CH_3 asym. bnd.	20.1 ± 0.2	43.3 ± 0.8	18.0 ± 0.2	45.0 ± 0.2
6.946	Aliph. CH_2, CH_3 asym. bnd.	2.2 ± 0.1	4.7 ± 0.2	0.0 ± 0.1	0.0 ± 0.1
7.000	Arom. CH bnd.	4.8 ± 0.4	9.7 ± 0.6	1.6 ± 0.1	4.2 ± 0.3
7.090	Olef. CH_2 bnd.	0.7 ± 0.3	1.5 ± 0.4	0.5 ± 0.1	1.0 ± 0.2
7.269	Aliph. CH_3 sym. bnd.	5.3 ± 1.2	11.9 ± 2.3	5.7 ± 0.3	14.1 ± 0.7

Table A.3. Integrated intensities of the features and components appearing in the ratios of Table 1, in units of 1×10^{-17} W/m^2.

Feature	IRAS 05073 (D1)	IRAS 06111 (D1)	J004441 (D2)	IRAS 05110 (D2)
3.3	2.4 ± 0.1	3.6 ± 0.1	2.3 ± 0.1	1.3 ± 0.2
3.38	1.11 ± 0.05	2.23 ± 0.06	0.72 ± 0.04	0.86 ± 0.06
3.42	2.70 ± 0.03	5.01 ± 0.05	1.44 ± 0.04	1.30 ± 0.05
3.4	8.2 ± 0.2	15.5 ± 0.3	4.4 ± 0.2	4.5 ± 0.3
Σ(3.3, 3.4)	10.6 ± 0.3	19.1 ± 0.4	6.7 ± 0.3	5.9 ± 0.5
6.2	28.4 ± 0.8	53.0 ± 1.0	18.3 ± 0.4	32.4 ± 0.6
6.9 aliph	25.8 ± 0.5	55.8 ± 1.3	20.2 ± 0.4	51.1 ± 0.4
6.9	31.4 ± 1.3	67.0 ± 2.3	22.3 ± 0.6	56.3 ± 1.0
7.25	5.3 ± 1.2	11.9 ± 2.3	5.7 ± 0.3	14.1 ± 0.7
11.2	45.2 ± 0.9	75.7 ± 1.2	26.9 ± 0.4	58.1 ± 0.8